



LAWRENCE
LIVERMORE
NATIONAL
LABORATORY

LLNL-JRNL-635881

Comparisons of angularly and spectrally resolved Bremsstrahlung measurements to 2-D multi-stage simulations of short-pulse laser-plasma interactions

C. D. Chen, A. J. Kemp, F. Perez, A. Link, F. N. Beg, S. Chawla, M. H. Key, H. McLean, A. Morace, Y. Ping, A. Sorokovikova, R. B. Stephens, M. Streeter, B. Westover, P. K. Patel

April 30, 2013

Physics of Plasmas

Disclaimer

This document was prepared as an account of work sponsored by an agency of the United States government. Neither the United States government nor Lawrence Livermore National Security, LLC, nor any of their employees makes any warranty, expressed or implied, or assumes any legal liability or responsibility for the accuracy, completeness, or usefulness of any information, apparatus, product, or process disclosed, or represents that its use would not infringe privately owned rights. Reference herein to any specific commercial product, process, or service by trade name, trademark, manufacturer, or otherwise does not necessarily constitute or imply its endorsement, recommendation, or favoring by the United States government or Lawrence Livermore National Security, LLC. The views and opinions of authors expressed herein do not necessarily state or reflect those of the United States government or Lawrence Livermore National Security, LLC, and shall not be used for advertising or product endorsement purposes.

Comparisons of angularly and spectrally resolved Bremsstrahlung measurements to 2-D multi-stage simulations of short-pulse laser-plasma interactions

C.D. Chen,^{1, a)} A.J. Kemp,¹ F. Pérez,¹ A. Link,¹ M.H. Key,¹ Y. Ping,¹ F.N. Beg,² S. Chawla,² H. McLean,¹ A. Morace,³ A. Sorokovikova,² R.B. Stephens,⁴ M. Streeter,⁵ B. Westover,² and P.K. Patel¹

¹⁾ *Lawrence Livermore National Laboratory*

²⁾ *University of California, San Diego*

³⁾ *University of Milan^{b)}*

⁴⁾ *General Atomics*

⁵⁾ *Imperial College London*

(Dated: 15 April 2013)

A 2-D multi-stage simulation model incorporating realistic laser conditions and a fully-resolved electron distribution handoff has been developed and compared to angularly and spectrally resolved Bremsstrahlung measurements from high-Z planar targets. For near-normal incidence and $0.5 - 1 \times 10^{20}$ W/cm² intensity, PIC simulations predict the existence of a high energy electron component consistently directed away from the laser axis, in contrast with previous expectations for oblique irradiation. Measurements of the angular distribution are consistent with a high energy component when directed along the PIC predicted direction, as opposed to between the target normal and laser axis as previously measured.

I. INTRODUCTION

Since the advent of chirped pulse amplification¹, short-pulse lasers have become important tools in the field of high energy density physics, serving as sources of relativistic electrons for a wide variety of applications such as particle accelerators², proton beams³, positron sources⁴, x-ray backlighters⁵, creating states of isochoric warm dense matter⁶, and serving as a fusion ignitor beam for the fast ignition (FI) concept⁷. Extensive experimental and computational efforts over the years have taught us a great deal about the physics of laser-plasma interactions at these relativistic intensities. Recently, efforts have been made to quantitatively compare simulations to experiments in small targets, where computational resource demands are relaxed^{8,9}. Currently, however, no reliable, well-benchmarked predictive capability exists for quantitative calculations of the characteristics of the hot electron distribution. A benchmarked code capability is important for interpreting experimental results, and is critical in applications such as fast ignition, where an ignition design requires scaling to conditions beyond those of existing laser facilities¹⁰.

In recent years, increased recognition of the importance of the effects of preformed plasma¹¹ and high-current transport physics^{12,13} have led to multi-stage simulation models becoming the gold standard for comparisons of particle-in-cell (PIC) simulations to experimental data for large targets. These simulations typically consist of a 2-D cylindrical hydrodynamic simulation for modeling the preformed plasma profile generated by the amplified spontaneous emission (ASE) prepulse, a 2-D

cartesian PIC simulation for modeling the laser-plasma interaction and electron generation, and a 2-D cylindrical or 3-D hybrid-PIC transport code to model the transport of the high-current electron beam through dense targets. Simulations are often performed under idealized conditions, such as a normal incident beam with a gaussian focal spot, when the actual laser is aberrated with near-normal incidence. Hydrodynamic simulations are also often omitted in favor of a simple exponential preformed plasma profile. In addition, the handoff between the PIC and hybrid-PIC transport code is often simplified, usually consisting of a time-integrated energy distribution, a total conversion efficiency, and a total time-integrated angular divergence, sometimes characterized by just a single parameter. While these approaches have been very successful in reproducing experimental trends^{14,15,16,17}, a quantitative comparison to data requires a more rigorous approach. These comparisons also require significant attention to laser characterization during experimental campaigns, which can be a challenge with limited time and resources.

The primary source parameters include the laser to electron conversion efficiency, the spatial flux profile, the energy spectrum, and the angular distribution of the electron beam. Recent studies have shown that the angular distribution is the key parameter determining coupling to the FI pre-compressed core¹⁰, from a ballistic transport standpoint as well as in determining the degree of magnetic beam collimation^{18,19,20,10}. Previous experimental techniques for measuring the electron divergence have primarily made use of K α imaging of buried fluors^{21,22,23}, although other techniques such as side-on K α fluors, angular Bremsstrahlung measurements^{24,25,26}, proton imaging^{27,28}, and measurements of surface heating and transition radiation^{20,23,29,30} have also been used.

In this paper we propose a method to compare the re-

^{a)} chen41@llnl.gov

^{b)} University of California, San Diego

sults of a 2-D multi-stage simulation to angularly and spectrally resolved Bremsstrahlung measurements in order to constrain the predicted hot electron distribution generated in the laser-plasma interaction. The measurements were coupled with a suite of laser diagnostics to characterize the laser conditions for realistic modeling of the laser-plasma interaction (LPI). A 2-D multi-stage simulation model has been developed based on measured laser conditions. The simulation model also incorporates a fully resolved handoff between the PIC and hybrid-PIC simulation, passing 4-D electron distributions resolved in time, space, energy, and angle. From the simulations we find that, for a 10^{20} W/cm² laser at near-normal incidence, the electron distribution breaks down into a symmetric, lower energy component, and a high energy, off-axis electron component. The off-axis component is consistently directed away from the laser axis, and not between the target normal and laser axis directions³¹, nor stochastically directed²⁵, as previously found. Transport simulations varying the direction of the high energy component show that this component must be directed along the direction predicted by PIC for consistency with the Bremsstrahlung measurements, and not between the target normal and laser axis as expected prior to the experiment.

Section 2 of this paper describes the experiments. Section 3 discusses the PIC simulation and characterization of the resulting electron distribution. Section 4 describes the transport simulation and the transfer process between the PIC and hybrid-PIC. Section 5 compares the simulations to experimental results and discusses the differences. Section 6 presents conclusions and future work that will help refine these comparisons.

II. EXPERIMENTAL MEASUREMENTS

The experiments were performed on the Titan laser at LLNL. Titan is a Nd:glass 1.053 μ m laser (150 J, 0.7 ps) focused with an f/3, 16° off-axis parabola. The laser was incident on target at 16° with s-polarization. The laser diagnostics included a 12-bit CCD for imaging the vacuum focal spot at low power, an equivalent plane monitor with a full aperture 6.3 m focal length lens for imaging the on shot focal spot variation, a 2nd harmonic frequency-resolved optical gating (FROG) diagnostic for measuring the pulse length, and a water-cell-protected photodiode for measuring the prepulse ($t_{res} = 100$ ps, 5 ns window). The focal spot can vary shot-to-shot through the day due to thermal distortions in the amplifier. Typical laser parameters consisted of an aberrated 7 μ m full width half maximum (FWHM) spot which contained 15% of the energy and a pulselength between 0.6-0.8 ps FWHM. The shot-to-shot thermal variation results in peak intensities between 5×10^{19} - 1×10^{20} W/cm². Prepulses ranged from 5-20 mJ in a 2.3 ns pedestal with most shots around 11 mJ.

The targets were 10 μ m Al/ 500 μ m Ag planar foils,

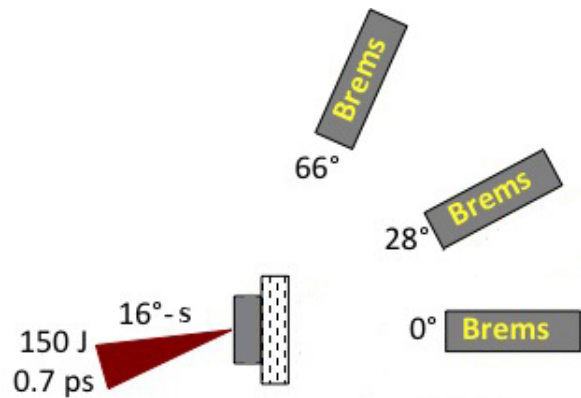


FIG. 1. Experimental Layout

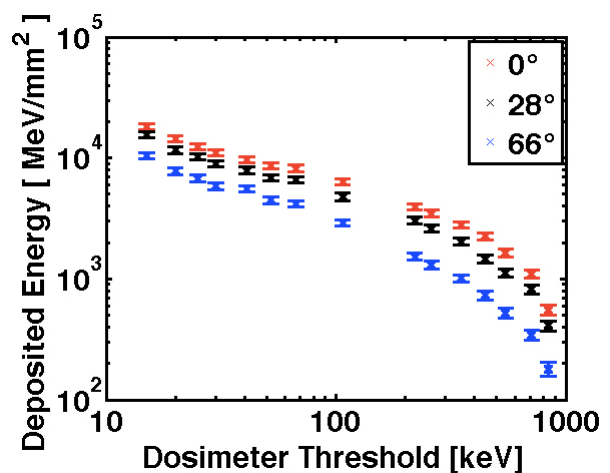


FIG. 2. Bremsstrahlung data showing the dose on each channel plotted against the threshold energy for that channel. Note that the dosimeter sensitivity extends significantly beyond the threshold.

backed by a 1 mm thick polystyrene layer to reduce electron refluxing. Lateral dimensions on both targets were 1 mm x 1 mm for the metal foils and 5 mm x 5 mm for the get-loss layer, whose large lateral dimension reduces electron refluxing through the front layers.

The experimental setup is shown in Figure 1. Bremsstrahlung emission was measured with an array of 3 absolutely-calibrated filter-stack spectrometers³² with spectral resolution thresholds from 10 keV-800 keV in 15 channels. Photon energies above 800 keV deposit energy in each channel but are not distinguishable. Each spectrometer had a magnet placed in front to eliminate electron contamination up to 100 MeV. The spectrometer response has been updated from the reference with a full 3 dimensional response model because the original 1 dimensional model overestimated the response to photons > 1 MeV by up to a factor of 2.

Figure 2 plots the raw Bremsstrahlung spectrometer signals for each of the 3 spectrometers. The response

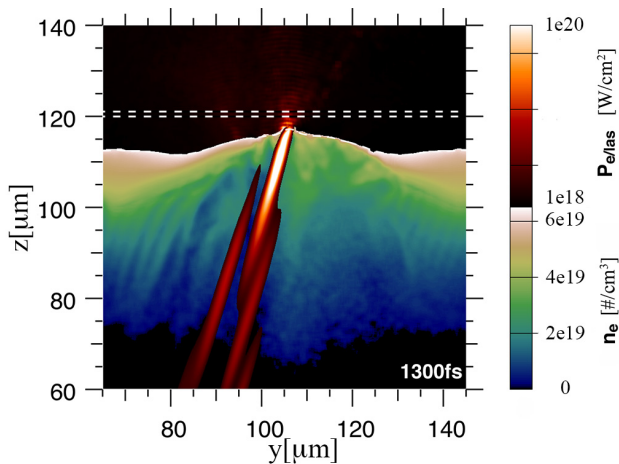


FIG. 3. Snapshot of the PIC simulation at peak power. The Poynting flux and background electron density are shown in the bottom section of the plot. The hot electron energy flux is plotted in the top section. The electron distribution is measured in a $1 \mu\text{m}$ box at $z = 120 \mu\text{m}$.

function of each spectrometer channel is extremely broad; in this figure the channel data is plotted against the threshold sensitivity. The slope encodes information about the electron spectrum up to a few MeV since photons up to 800 keV are primarily generated by few MeV electrons. As each spectrometer is placed at a different angle, the ratio between the spectrometers provides information about the angular distribution of the Bremsstrahlung emission, which correlates with the electron angular distribution.

III. PIC SIMULATIONS

Two dimensional simulations in cartesian geometry of the laser-plasma interaction (LPI) were performed with the PIC code PSC^{33,34}. The simulation is run in a fully kinetic mode with two spatial and three velocity dimensions (2D-3V). The simulation grid is 180 (transverse) \times 150 μm (axially) with 32 cells/ μm in each dimension and 74 steps/laser cycle. There are 50 electrons and 50 ions per cell. The plasma profile is initialized from a 2-D hydrodynamic simulation in cylindrical geometry using the HYDRA code with a 12 mJ prepulse in 2.3 ns, with exact temporal profiles taken from the prepulse monitor. Ionization states imported from the HYDRA profile are fixed, and the background density is capped at 100x the critical density for $1 \mu\text{m}$ wavelength. The boundary conditions are periodic on the sides and absorbing at the rear.

2-D Cartesian simulations cannot simultaneously match both the spatial profile and intensity distribution of the actual laser focal spot because the laser is represented as a line profile without the appropriate cylindrical area weighting. To most accurately represent the focal spot of the Titan laser, the laser source in these simula-

tions is initialized with an $f/3$ beam and a random phase profile that reproduces the measured intensity distribution from 10^{17} - 10^{20} W/cm^2 . The laser is injected at 16° incidence with p-polarization. While the experiment was s-polarized, we find that a 2-D p-polarized simulation is a better representation of an experiment with a laser prepulse. This is due to the main pulse forming a cavity at the interaction surface so that the laser electric field is directed normal to the plasma surface; this is not the case for 2-D simulations of s-polarized beams, in which the laser electric field is always parallel to the plasma surface. The temporal profile is a 0.7 ps FWHM gaussian and the simulation is run for 2.0 ps. A snapshot of the simulation is shown in Figure 3 at peak laser power, with the background electron density, laser Poynting flux, and hot electron energy flux included on the colormap. Simulations are run at 1×10^{20} nominal intensity [baseline] and 5×10^{19} W/cm^2 [half intensity] in order to bracket the range in the laser intensity during the experiment.

The electron distribution is sampled every 20 fs in a $1 \mu\text{m}$ thick box at $z = 120 \mu\text{m}$, just behind the interaction surface (see dashed lines in Figure 3). To prevent double counting, the electrons in the box are weighted by their velocity component perpendicular to the measurement line to account for longer transit time of slower electrons; this effectively calculates a flux through the box. The isotropic thermal electron component is removed by subtracting oppositely directed electrons of the same energy $f(E, \theta) = f(E, \theta) - f(E, \theta + \pi)$, where E is the electron energy and θ is the angle with respect to the normal. This isotropic thermal component serves only as a heated background and is removed to maximize statistical sampling of the supra thermal electrons in the hybrid-PIC transport code. The return current is not affected because it is a backward-going distribution above the symmetric background. For sufficient statistical representation, the 4-D distribution (time, space, energy, angle) is separated in the following way. The energy distribution is sampled as a function of space in 0.5 μm spatial bins and 200 log-spaced energy bins from 1 keV - 60 MeV. The angular distribution and spatial flux are also spatially resolved, but energy resolution of these quantities is in 10 log spaced bins up to 60 MeV since these quantities are slowly varying with energy.

The time integrated distributions are shown in Figure 4. Figure 4a plots the energy distribution for the two simulations with $T_{\text{hot}} = 7.0$ MeV, for the baseline case, and $T_{\text{hot}} = 5.1$ MeV for the half intensity case. These slope temperatures are 2.7-2.9x the vacuum ponderomotive temperature, whereas in the simulation the laser self-focuses to 2.2x the peak vacuum intensity. This suggests that under-dense interactions in the preformed plasma are primarily responsible for the electrons in the hot tail. The spatial flux distribution of the baseline simulation is shown for the same energy bands in Figure 4b. There are two electron sources, one broad source peaking at $107 \mu\text{m}$, where the laser is pointed, and a narrow source component peaking at $99 \mu\text{m}$.

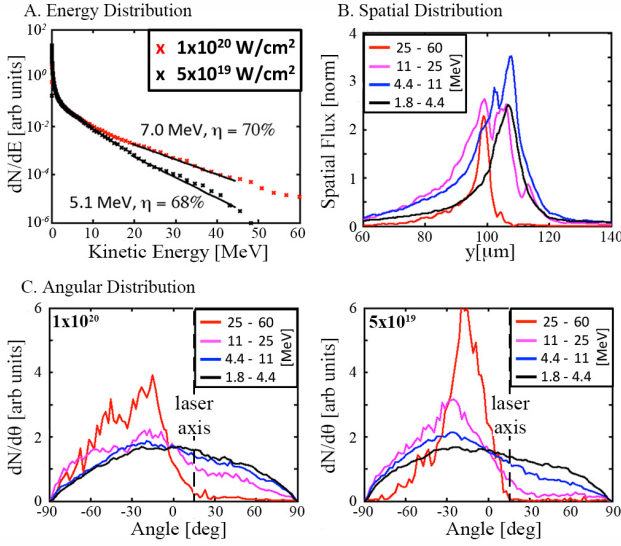


FIG. 4. Characteristics of the time-integrated electron distributions from the PIC simulation. a) Energy spectrum b) Spatial flux. The symmetric component is the peak at 107 μm and the asymmetric component has a peak at 99 μm . c) Angular Distribution for different energy groups showing a high energy component directed away from the laser axis.

TABLE I. Comparison of PIC simulations.

I (W/cm^2)	1×10^{20}	5×10^{19}
$\eta_{L \rightarrow e^-}$	70%	68%
T_{hot} (MeV)	7.0	4.8
$\langle \theta \rangle_{\text{asym}}$	$-30^\circ \pm 2$	$-37^\circ \rightarrow -20^\circ$
$\Delta\theta_{\text{asym}}$	$20^\circ \pm 1$	$20^\circ \pm 1$
$\Delta\theta_{\text{sym}}$	$31^\circ \pm 3$	$31^\circ \pm 3$
f_{asym}	22%	32%

$\eta_{L \rightarrow e^-}$	conversion efficiency
$\langle \theta \rangle_{\text{asym}}$	mean direction
f_{asym}	fraction asymmetric

The angular distribution is characterized in 10 logarithmic energy bands, and four of these are shown in Figure 4c. There are two components to the hot electron distribution: (i) a symmetric, broad, forward directed component, and (ii) an asymmetric high-energy component directed away from the laser axis. They are spatially separated as seen in Figure 4b. The asymmetric component is more sharply peaked for the half intensity simulation and the asymmetry extends to lower energies. In the half intensity simulation the symmetric component shifts to lower energy, resulting in a more skewed distribution at high energies (the asymmetric shifts as well but has a higher mean energy) compared to the baseline intensity distribution.

The distributions are characterized in Table I. The total conversion efficiency into forward going hot electrons is 68-70%. The angular distribution of the symmetric component is flat across all energies at both intensities,

with $\Delta\theta = 31^\circ$, which is defined as the average absolute deviation about the mean (about 0° for the symmetric component, about the mean direction for the asymmetric component). The asymmetric component is narrower: $\Delta\theta = 20^\circ$ for both simulations. In the baseline simulation, the asymmetric component consists primarily of electrons greater than 10 MeV, whereas at half intensity electrons down to 4 MeV are in the asymmetric component. For the baseline simulation, the high-energy component is directed at -30° , while for the half intensity simulation the directionality varies from -37° at 4 MeV to -20° at >25 MeV.

IV. HYBRID-PIC ELECTRON TRANSPORT SIMULATIONS

Electron transport simulations are performed with the hybrid-PIC code Zuma³⁵. A detailed description of the transport physics contained within Zuma is described by Strozzi, et. al.¹⁰. The Zuma model uses kinetic electrons on top of a fixed background plasma. The electric field is calculated from Ohm's law using an unmagnetized Lee-More³⁶ resistivity model with Dejarlais³⁷ extension (LMD). Drag and scattering formulas are taken from Solodov and Betti³⁸ and Davies^{39,40}. The background plasma uses an ideal gas equation of state (EOS) and ionization according to Desjarlais³⁷ blend between pressure-ionization-corrected Saha and Thomas-Fermi ionization models. For Bremsstrahlung generation and radiative energy loss, cross sections from the Integrated Tiger Series 3.0 (ITS 3.0)⁴¹ are incorporated into the transport model, including photon generation and impact ionization generation of secondary electrons. ITS Photon transport is not incorporated; instead, opacities are post-processed using cold matter x-ray mass attenuation coefficients from NIST⁴². Open boundary conditions are used at all surfaces: electrons that leave the target are removed from the simulation.

The Zuma code is run in two modes in order to maximize computational efficiency. A 2-D cylindrical (RZ) simulation is used to model the symmetric component of the hot electrons. The asymmetric component represents 22% of the electron energy and contributes significantly to the Bremsstrahlung emission. Since the off-axis directionality cannot be accurately simulated in RZ geometry, a 3-D simulation in cartesian geometry is run for the asymmetric component. The 2-D RZ simulation is run with 1 μm grid resolution. For the 3-D simulations, since Zuma is not currently configured for 2-D division of its computational domains, full-scale 3-D simulations are currently impractical for a fully resolved grid. Therefore, the 3-D simulations are run without self-generated fields to save computational time and memory resources. This quantitatively reproduces the angular Bremsstrahlung distribution but physics such as beam filamentation are not included.

Mapping the distribution from a 2-D Cartesian LPI

simulation to a source for 2-D RZ or 3-D transport simulations mirrors the choice in initializing the laser in a 2-D LPI simulation. In the 2-D Cartesian LPI simulation the laser intensity distribution and spatial profile cannot simultaneously match the actual focal spot; the 2-D RZ and 3-D transport simulations cannot simultaneously match the electron energy spectrum and spatial flux profile from the 2-D Cartesian PIC simulation. The choice of matching the flux profile or the energy spectrum therefore modifies the electron distribution function with either $f(t, E, \theta|y) = f(t, E, \theta|r)$ or $f(t, E, \theta|y) dy = f(t, E, \theta|r) 2\pi r dr$, respectively. Matching the flux profile with $f(r) = f(y)$, for example, underweights the hot center and overweights the colder wings, resulting in a colder energy distribution than the 2-D simulation predicts. The most appropriate choice is the one correlated with the choice made for the LPI simulation. Since the LPI simulation is initialized such that the intensity distribution correlated with that of the experimental focal spot, mapping from 2-D Cartesian to 2-D RZ should conserve the electron energy distribution.

This choice is complicated by three details: (1) the high energy component originates from a wide source in the underdense plasma, complicating the contribution of this component to the spatial and angular distributions, (2) the laser and electron spatial profiles do not exactly correlate, and (3) the experimental focal spot was aberrated and not cylindrically symmetric. For these simulations, the following choices are made. The electron energy distribution is kept identical to the 2-D PIC prediction as previously discussed. Since the spatial spot is created from a random phase profile, there is little correlation to the spatial profile of the laser. Using the same transform on the spatial spot results in an unrealistically narrow source in RZ geometry because the aberrated spot is mapped to a perfectly cylindrical source. Thus, the spatial distribution in the cylindrical simulation is equated to that of the cartesian simulation ($f(r) = f(y)$).

As shown in Figure 4, the volumetric source of the high energy component leads to a broad wing and a secondary peak to the left of the focal spot. In 3-D geometry, however, this off-axis component is likely to be represented by a directional beam(s) rather than covering the half the solid angle or broadening the entire focal spot as a direct 2-D Cartesian to RZ mapping would require. Simulations were therefore also run with the radial spatial profile mapped using only the right side of the peak of the symmetric component ($f(y:107-180 \mu m) = f(r)$). However, for Bremsstrahlung measurements of high Z targets, scattering is significant and emission from high energy electrons are dominant; field effects do not significantly influence the results. Hence, modification of the spatial profile, and thus the current density, has little impact in this regime.

The injected electron angular distribution is mapped directly from the 2-D PIC simulation. The angular dependence is integrated over space because a spatial

weighting of the off-axis component would lead to an unphysical injection of a hollow cone in RZ geometry. This actually alters the spatial current profile. Debayle, et. al.⁴³ found that spatially integrating the angular distribution results in an overestimate of the beam collimation due to the neglect of the "radial drift", or spatial dependence of the transverse velocity component. Since collimating fields are not significant in these simulations this effect does not come into play, but would be important in simulations of low Z targets or of diagnostics where low energy electrons play a major role (i.e. $K\alpha$).

As previously discussed, the symmetric component of the angular distribution is injected in RZ geometry, whereas the asymmetric component is injected with off-axis directionality in a 3-D Cartesian simulation. The off-axis component direction in the 3-D simulations is varied from 0-50° in 5° increments. The off-axis directionality is thus modeled by sampling the Bremsstrahlung in θ and ϕ in the 3-D simulation.

Overall, an exact prescription is not possible until 3-D PIC simulations are compared to 2-D counterparts. 3-D PIC simulations by F. Pérez have recently been completed and comparisons are under way to further explore this distribution mapping.

V. COMPARISONS TO BREMSSTRAHLUNG MEASUREMENTS

Simulated Bremsstrahlung signals are obtained by summing the Bremsstrahlung emission from the 2-D RZ & 3-D Cartesian transport simulations, applying cold matter opacity corrections, and folding the spectrum with the spectrometer response function. The simulated data is plotted against the measurements in Figure 5. Synthetic data from two simulations are shown: the nominal intensity simulation and the half intensity simulation, with the off-axis component pointed at -30° and -25°, respectively, in the equatorial plane.

Figure 5a breaks down the signal by the initial electron energy at injection for the half intensity simulation. The contribution from the off-axis component is separately identified. The Bremsstrahlung signals are primarily produced by electrons above >2 MeV, although electrons between 0.3-2 MeV contribute to the lower channels. The last few channels represent only electrons >4 MeV. With the off-axis component pointed in the -25° direction, it contributes more to the 0° and 28° spectrometers. The contribution from 10-25 MeV electrons is low because the are primarily accounted for in the off-axis component.

Figure 5b normalizes the simulated signals to the data in order to visualize the difference in the spectrum and coupling efficiency. The simulated slope and absolute signals in the rear 9 channels of the half intensity simulation are in good agreement with the Bremsstrahlung measurements, whereas they are both significantly higher for the nominal intensity simulation. Note that this agreement only holds when the off-axis component is directed along

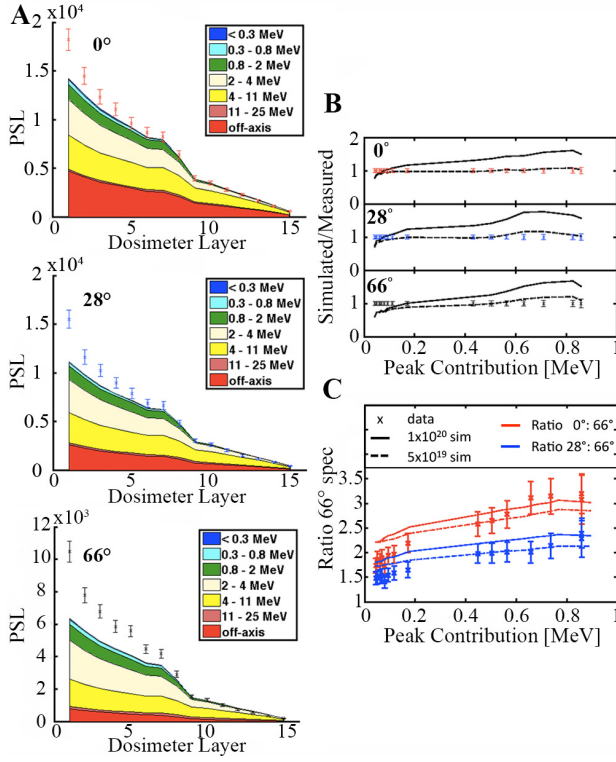


FIG. 5. a) Bremsstrahlung signals from the 5×10^{19} W/cm² simulation are broken down by original electron energy and plotted against measurements. b) Simulated signals are normalized to the respective measured signals to visualize spectrum temperature and coupling efficiency for the two simulations, baseline (solid) and half intensity (dashed). c) Simulated and measured ratios between different spectrometers are plotted for visualization of the electron divergence for the two simulations. Solid lines and dashed lines represent the nominal and half intensity cases, respectively. Red and blue represent the ratios of 0°:66° and 28°:66°, respectively.

the PIC predicted direction; the slope deviates significantly along other directions. The Bremsstrahlung spectrometers are able to differentiate between the two predicted T_{hot} for these specific laser and target conditions (thick, high Z, 10^{19} - 10^{20} W/cm²). The conversion efficiency is also in good agreement assuming that a large fraction of the energy is directed away from the spectrometers as PIC predicts. The predicted signals are lower than the measured signals for the first 6 channels, which, as can be inferred from Figure 5a, is likely due to electrons < 2 MeV. This could be due to a number of factors, including issues with the PIC prediction for low energy electrons, or the open boundary conditions in the Zuma simulation. Because Zuma cannot self-consistently calculate surface fields, electrons that leave the target are removed. It is possible that some fraction of the low energy escaping electrons reflux back into the target, producing additional Bremsstrahlung.

Figure 5c plots the ratios between different spectrometers. Higher ratios representing narrower divergence.

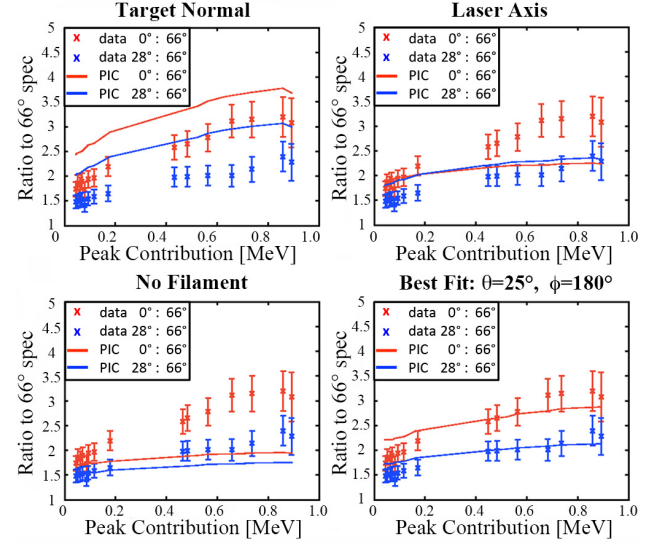


FIG. 6. Bremsstrahlung spectrometer ratios for the half intensity case for 4 cases for the high energy component: directed along target normal, directed along laser axis, no high energy component, and the best fit direction.

The ratios isolate the divergence information from the spectrometers even if the energy spectrum is somewhat incorrect (although large errors in the energy spectrum influence the inferred divergence due to the coupled angular and energy dependence of the Bremsstrahlung cross section). The predicted off-axis direction leads to a reasonably good fit for the ratios at high energies for both simulations, showing the even if the slope temperature is too high in the nominal case, the consistency of the predicted off-axis beam direction with the measurements holds true for both cases. Both ratios are too high at low energies, suggesting there are insufficient numbers of low energy photons at wide angles. This again may be due to inaccuracies in the PIC predicted low energy angular distribution, or the neglect of low energy electron refluxing. A self-consistent boundary field is currently beyond the capability of the Zuma code.

As previously discussed, the off-axis high-energy component was simulated for various injection directions. For the half intensity case, Figure 6 shows the ratios for 4 scenarios: the high energy component directed along the target normal, laser axis, no high energy component, and the best fit direction. With the high energy component is directed on axis, the signal on the forward channels is significantly too high. Along the laser axis, brings the ratio numbers down but inverts the signal ratios on the 0° and 28° spectrometers. Excluding the asymmetric component entirely results in an angular distribution that is much too broad to fit the data. The best fit provides a good representation to the high energy ratios, while being somewhat too high for the low energy ratios, for reasons previously discussed.

The data is therefore consistent with a high energy

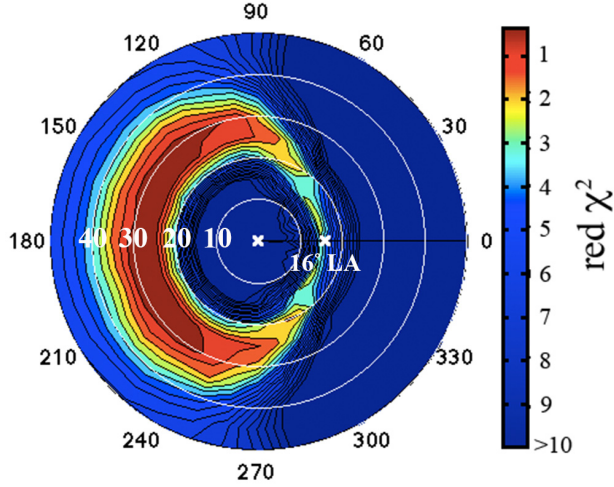


FIG. 7. Reduced χ^2 fitting parameter for the half intensity case as a function of the hot electron beam direction. The radial coordinate is θ and the azimuthal coordinate is ϕ . The target normal and laser axis directions are marked with white crosses, at the center and at $\theta = 16^\circ$, $\phi = 0^\circ$, respectively.

component directed away from the laser axis, as predicted by the PIC simulations. The full directionality parameter space was explored by varying the direction of the high energy component and calculating the fitting parameter to the ratios. Only the rear 9 channels were used since we are primarily interested in the high-energy electrons.

Figure 7 plots the reduced- χ^2 fitting parameter for the half intensity case as a function of θ and ϕ , where θ is the angle to target normal and ϕ is its azimuthal angle. The target normal and laser axis references are marked by white crosses, at $\theta = 0^\circ$ and $\theta = 16^\circ$, $\phi = 0^\circ$, respectively. For reference, the laser is polarized in the $\phi = 90^\circ$ direction (the beam direction was varied only for the transport simulation and not the PIC simulation). The best fit for the off-axis pointing is between $\theta = 24^\circ - 31^\circ$ and $\phi = 120^\circ - 240^\circ$, away from the laser axis, which is consistent with the PIC prediction.

VI. DISCUSSION

The physical origin of the asymmetric component directionality is still under investigation, but one possible explanation is that strong magnetic fields ($B = 300$ MG) appear in the underdense plasma in front of the target, and cause the electron beam to be deviated away from the laser axis. Several mechanisms can generate such fields, including the strong currents from electron acceleration, the thermoelectric effect $\nabla T \times \nabla n$ ⁴⁴, (T = electron temperature, n = density), and other effects directly related to the laser interaction^{45,46,47}. They are fairly independent of the polarization of the laser. Electrons above a few MeV are more sensitive to these fields as they gen-

erally spend longer time in the pre-plasma region. Consequently, they get significantly deviated away from the laser axis. This mechanism and directionality is different from what has been seen before by Santala, et. al.³¹ both computationally and experimentally at more oblique incidence (45°). Their simulations of beam directionality were shorter than 100 fs, before the surface B field had time to grow, and thus this effect may not be present. In our simulations, the electrons do propagate along the laser axis at early time, but switch direction after 200 fs, during the rising edge of the pulse of the present experiment. Previous experimental results by Schwoerer, et. al.²⁴, Santala, et. al.³¹, Norreys, et. al.²⁶, and Cho et. al.⁴⁸ showing the electron beam on the laser axis were performed at 45° incidence and $1-3 \times 10^{19}$ W/cm² laser intensities. We have performed simulations under those conditions that replicate the beam directed along the laser axis. At such lower intensities and larger incidence angles, the high energy electrons are not trapped by the surface B fields and propagate along the laser axis direction. Thus, our simulations suggest that closer-to-normal incidence, higher intensities, and longer pulses have an important impact on the electron beam direction. Additional spectrometers covering a larger solid angle, however, would be able to provide direct verification of this directionality change.

To verify that this is not a numerically stochastic phenomenon, as well as to sample the uncertainty in the simulated distribution parameters, two additional simulations at 1×10^{20} W/cm² were performed with different random seeds and phase initializations. While there were small variations in T_{hot} (6.3 - 7.0 MeV), the angular widths of both the components remained the same and the asymmetric component directionality varied only slightly from $30^\circ - 35^\circ$.

Conclusive proof of the off-axis high energy component direction in near-normal incidence conditions requires more spectrometers covering wider solid angles. We cannot currently rule out that another distribution with completely different angular, spectral, and conversion efficiency characteristics does not provide a degenerate solution to the Bremsstrahlung measurements. However, current measurements are in agreement with the PIC prediction, and another degenerate solution would have to have parameters significantly different from the one predicted by the PIC simulations. Increased shot statistics would also be useful in examining the experimental stochasticity of the high energy component directionality under these conditions, although in this case, two shots were taken with similar results. Since the divergence measurements are dominated by this high energy component, angular comparisons of the symmetric component also require better angular coverage. Additionally, while a reasonable 2-D to 3-D distribution mapping was used, validation of this technique and quantification of its associated errors require detailed comparisons to 3-D PIC simulations.

VII. CONCLUSIONS

A 2-D multi-stage simulation model using realistic laser conditions and a fully resolved electron distribution handoff has been compared to angularly and spectrally resolved Bremsstrahlung measurements from irradiation of high Z planar targets. This method is more detailed and precise than the previous analyses of similar data. It significantly constrains the electron distribution and can be applied to future experiments featuring more advanced diagnostic designs. In the situation of the presented experimental results (16° incidence, $0.5\text{-}1\times 10^{20}$ W/cm²), the PIC simulations predict a high-energy off-axis electron component, consistently directed away from the laser axis. The experimental data strongly supports this predicted direction. Additional experiments measuring Bremsstrahlung spectra over wider angles will help further constrain the electron angular distribution and confirm the energy fraction directed away from the spectrometers. 3-D PIC simulations by F. Pérez have recently been completed and these support the physics of the off-axis component. Detailed comparisons are underway to understand the 2-D to 3-D mapping of the electron distribution.

ACKNOWLEDGMENTS

The authors would like to acknowledge Rick Freeman for useful discussions during the experiments, as well as the staff of the Jupiter Laser Facility at LLNL for their assistance and support. This work was performed under the auspices of the U.S. Department of Energy by Lawrence Livermore National Laboratory under Contract No. DE-AC52-07NA27344.

- ¹D. Strickland and G. Mourou, *Optics Communications* **55**, 447 (1985).
- ²W. P. Leemans, B. Nagler, A. J. Gonsalves, C. Toth, K. Nakamura, C. G. R. Geddes, E. Esarey, C. B. Schroeder, and S. M. Hooker, *Nature Physics* **2**, 696 (2006).
- ³R. A. Snavely, M. H. Key, S. P. Hatchett, T. E. Cowan, M. Roth, T. W. Phillips, M. A. Stoyer, E. A. Henry, T. C. Sangster, M. S. Singh, S. C. Wilks, A. MacKinnon, A. Offenberger, D. M. Pennington, K. Yasuike, A. B. Langdon, B. F. Lasinski, J. Johnson, M. D. Perry, and E. M. Campbell, *Phys. Rev. Lett.* **85**, 2945 (2000).
- ⁴H. Chen, S. C. Wilks, J. D. Bonlie, E. P. Liang, J. Myatt, D. F. Price, D. D. Meyerhofer, and P. Beiersdorfer, *Phys. Rev. Lett.* **102**, 105001 (2009).
- ⁵H.-S. Park, D. M. Chambers, H.-K. Chung, R. J. Clarke, R. Egleton, E. Giraldez, T. Goldsack, R. Heathcote, N. Izumi, M. H. Key, J. A. King, J. A. Koch, O. L. Landen, A. Nikroo, P. K. Patel, D. F. Price, B. A. Remington, H. F. Robey, R. A. Snavely, D. A. Steinman, R. B. Stephens, C. Stoeckl, M. Storm, M. Tabak, W. Theobald, R. P. J. Town, J. E. Wickersham, and B. B. Zhang, *Physics of Plasmas* **13**, 056309 (2006).
- ⁶K. Widmann, T. Ao, M. E. Foord, D. F. Price, A. D. Ellis, P. T. Springer, and A. Ng, *Phys. Rev. Lett.* **92**, 125002 (2004).
- ⁷M. Tabak, J. Hammer, M. E. Glinsky, W. L. Kruer, S. C. Wilks, J. Woodworth, E. M. Campbell, M. D. Perry, and R. J. Mason, *Physics of Plasmas* **1**, 1626 (1994).

- ⁸Y. Sentoku, E. d'Humières, L. Romagnani, P. Audebert, and J. Fuchs, *Phys. Rev. Lett.* **107**, 135005 (2011).
- ⁹Y. Ping, A. J. Kemp, L. Divol, M. H. Key, P. K. Patel, K. U. Akli, F. N. Beg, S. Chawla, C. D. Chen, R. R. Freeman, D. Hey, D. P. Higginson, L. C. Jarrott, G. E. Kemp, A. Link, H. S. McLean, H. Sawada, R. B. Stephens, D. Turnbull, B. Westover, and S. C. Wilks, *Phys. Rev. Lett.* **109**, 145006 (2012).
- ¹⁰D. J. Strozzi, M. Tabak, D. J. Larson, L. Divol, A. J. Kemp, C. Bellei, M. M. Marinak, and M. H. Key, *Physics of Plasmas* **19**, 072711 (2012).
- ¹¹Y. Ping, R. Shepherd, B. F. Lasinski, M. Tabak, H. Chen, H. K. Chung, K. B. Fournier, S. B. Hansen, A. Kemp, D. A. Liedahl, K. Widmann, S. C. Wilks, W. Rozmus, and M. Sherlock, *Phys. Rev. Lett.* **100**, 085004 (2008).
- ¹²A. R. Bell, J. R. Davies, S. Guerin, and H. Ruhl, *Plasma Physics and Controlled Fusion* **39**, 653 (1997).
- ¹³J. R. Davies, *Phys. Rev. E* **65**, 026407 (2002).
- ¹⁴S. Wilks and W. Kruer, *Quantum Electronics, IEEE Journal of* **33**, 1954 (1997).
- ¹⁵G. Malka and J. Miquel, *Physical Review Letters* **77**, 75 (1996).
- ¹⁶J. Myatt, W. Theobald, J. A. Delettrez, C. Stoeckl, M. Storm, T. C. Sangster, A. V. Maximov, and R. W. Short, *Physics of Plasmas* **14**, 056301 (2007).
- ¹⁷P. M. Nilson, W. Theobald, J. Myatt, C. Stoeckl, M. Storm, O. V. Gotchev, J. D. Zuegel, R. Betti, D. D. Meyerhofer, and T. C. Sangster, *Physics of Plasmas* **15**, 056308 (2008).
- ¹⁸A. P. L. Robinson and M. Sherlock, *Physics of Plasmas* **14**, 083105 (2007).
- ¹⁹A. P. L. Robinson, M. Sherlock, and P. A. Norreys, *Physical Review Letters* **100**, 025002 (2008).
- ²⁰S. Kar, A. P. L. Robinson, D. C. Carroll, O. Lundh, K. Markey, P. McKenna, P. Norreys, and M. Zepf, *Physical Review Letters* **102**, 055001 (2009).
- ²¹R. B. Stephens, R. A. Snavely, Y. Aglitskiy, F. Amiranoff, C. Andersen, D. Batani, S. D. Baton, T. Cowan, R. R. Freeman, T. Hall, S. P. Hatchett, J. M. Hill, M. H. Key, J. A. King, J. A. Koch, M. Koenig, A. J. MacKinnon, K. L. Lancaster, E. Martinolli, P. Norreys, E. Perelli-Cippo, M. Rabec Le Gloahhec, C. Rousseaux, J. J. Santos, and F. Scianitti, *Phys. Rev. E* **69**, 066414 (2004).
- ²²F. Perez, M. Koenig, D. Batani, S. D. Baton, F. N. Beg, C. Benedetti, E. Brambrink, S. Chawla, F. Dorchies, C. Fourment, M. Galimberti, L. A. Gizzi, R. Heathcote, D. P. Higginson, S. Hulin, R. Jafa, P. Koester, L. Labate, K. Lancaster, A. J. MacKinnon, A. G. McPhee, W. Nazarov, P. Nicolai, J. Pasley, A. Ravasio, M. Richetta, J. J. Santos, A. Sgattoni, C. Spindloe, B. Vauzour, and L. Volpe, *Plasma Physics and Controlled Fusion* **51**, 124035 (2009).
- ²³K. L. Lancaster, J. S. Green, D. S. Hey, K. U. Akli, J. R. Davies, R. J. Clarke, R. R. Freeman, H. Habara, M. H. Key, R. Kodama, K. Krushelnick, C. D. Murphy, M. Nakatsutsumi, P. Simpson, R. Stephens, C. Stoeckl, T. Yabuuchi, M. Zepf, and P. A. Norreys, *Phys. Rev. Lett.* **98**, 125002 (2007).
- ²⁴H. Schwoerer, P. Gibbon, S. Dusterer, R. Behrens, C. Ziener, C. Reich, and R. Sauerbrey, *Phys. Rev. Lett.* **86**, 2317 (2001).
- ²⁵S. P. Hatchett, C. G. Brown, T. E. Cowan, E. A. Henry, J. S. Johnson, M. H. Key, J. A. Koch, A. B. Langdon, B. F. Lasinski, R. W. Lee, A. J. MacKinnon, D. M. Pennington, M. D. Perry, T. W. Phillips, M. Roth, T. C. Sangster, M. S. Singh, R. A. Snavely, M. A. Stoyer, S. C. Wilks, and K. Yasuike (AIP, 2000) pp. 2076–2082.
- ²⁶P. A. Norreys, M. Santala, E. Clark, M. Zepf, I. Watts, F. N. Beg, K. Krushelnick, M. Tatarakis, A. E. Dangor, X. Fang, P. Graham, T. McCanny, R. P. Singhal, K. W. D. Ledingham, A. Creswell, D. C. W. Sanderson, J. Magill, A. Machacek, J. S. Wark, R. Allott, B. Kennedy, and D. Neely, *Physics of Plasmas* **6**, 2150 (1999).
- ²⁷J. Fuchs, T. E. Cowan, P. Audebert, H. Ruhl, L. Gremillet, A. Kemp, M. Allen, A. Blazevic, J.-C. Gauthier, M. Geissel, M. Hegelich, S. Karsch, P. Parks, M. Roth, Y. Sentoku,

- R. Stephens, and E. M. Campbell, Phys. Rev. Lett. **91**, 255002 (2003).
- ²⁸M. Roth, M. Allen, P. Audebert, A. Blazevic, E. Brambrink, T. E. Cowan, J. Fuchs, J.-C. Gauthier, M. Geiel, M. Hegelich, S. Karsch, J. M. ter Vehn, H. Ruhl, T. Schlegel, and R. B. Stephens, Plasma Physics and Controlled Fusion **44**, B99 (2002).
- ²⁹J. S. Green, V. M. Ovchinnikov, R. G. Evans, K. U. Akli, H. Azechi, F. N. Beg, C. Bellei, R. R. Freeman, H. Habara, R. Heathcote, M. H. Key, J. A. King, K. L. Lancaster, N. C. Lopes, T. Ma, A. J. MacKinnon, K. Markey, A. McPhee, Z. Najmudin, P. Nilson, R. Onofrei, R. Stephens, K. Takeda, K. A. Tanaka, W. Theobald, T. Tanimoto, J. Waugh, L. Van Woerkom, N. C. Woolsey, M. Zepf, J. R. Davies, and P. A. Norreys, Phys. Rev. Lett. **100**, 015003 (2008).
- ³⁰P. Antici, B. Albertazzi, P. Audebert, S. Buffechoux, F. Hannachi, E. d'Humieres, F. Gobet, T. Grismayer, A. Mancic, M. Nakatsutsumi, C. Plaisir, L. Romagnani, M. Tarisien, H. Ppin, Y. Sentoku, and J. Fuchs, New Journal of Physics **14**, 063023 (2012).
- ³¹M. I. K. Santala, M. Zepf, I. Watts, F. N. Beg, E. Clark, M. Tatarakis, K. Krushelnick, A. E. Dangor, T. McCanny, I. Spencer, R. P. Singhal, K. W. D. Ledingham, S. C. Wilks, A. C. Machacek, J. S. Wark, R. Allott, R. J. Clarke, and P. A. Norreys, Phys. Rev. Lett. **84**, 1459 (2000).
- ³²C. D. Chen, J. A. King, M. H. Key, K. U. Akli, F. N. Beg, H. Chen, R. R. Freeman, A. Link, A. J. MacKinnon, A. G. MacPhee, P. K. Patel, M. Porkolab, R. B. Stephens, and L. D. V. Woerkom, Review of Scientific Instruments **79**, 10E305 (2008).
- ³³M. Bonitz, G. Bertsch, V. Filinov, and H. Ruhl, *Introduction to Computational Methods in Many Body Physics* (Rinton, Princeton, NJ, 2006) Chap. Chapter 2.
- ³⁴A. J. Kemp, B. I. Cohen, and L. Divol, Physics of Plasmas **17**, 056702 (2010).
- ³⁵D. Larson, M. Tabak, and T. Ma, "Hybrid simulations for magnetized fast ignition targets and analyzing cone-wire experiments," Bull. Am. Phys. Soc. 55 (2010).
- ³⁶Y. Lee and R. More, Physics of Fluids **27**, 1273 (1984).
- ³⁷M. Desjarlais, Contributions to Plasma Physics **41**, 267 (2001).
- ³⁸A. A. Solodov and R. Betti, Physics of Plasmas **15**, 042707 (2008).
- ³⁹J. Davies, "Fast electron stopping and scattering in fast ignition," Bull. Am. Phys. Soc. 53 (2008).
- ⁴⁰S. Atzeni, A. Schiavi, and J. R. Davies, Plasma Physics and Controlled Fusion **51**, 015016 (2009).
- ⁴¹J. Halbleib, R. Kensek, G. Valdez, S. Seltzer, and M. Berger, Nuclear Science, IEEE Transactions on **39**, 1025 (1992).
- ⁴²J. Hubbell and S. Seltzer, "Tables of x-ray mass attenuation coefficients and mass energy-absorption coefficients 1 keV to 20 MeV for elements $z = 1$ to 92 and 48 additional substances of dosimetric interest," Tech. Rep. PB-95-220539/XAB; NISTIR-5632 (National Institute of Standards and Technology, Gaithersburg, MD, 1995).
- ⁴³A. Debayle, J. J. Honrubia, E. d'Humières, and V. T. Tikhonchuk, Phys. Rev. E **82**, 036405 (2010).
- ⁴⁴J. A. Stamper, K. Papadopoulos, R. N. Sudan, S. O. Dean, E. A. McLean, and J. M. Dawson, Phys. Rev. Lett. **26**, 1012 (1971).
- ⁴⁵R. N. Sudan, Phys. Rev. Lett. **70**, 3075 (1993).
- ⁴⁶M. G. Haines, Canadian Journal of Physics **64**, 912 (1986), <http://www.nrcresearchpress.com/doi/pdf/10.1139/p86-160>.
- ⁴⁷R. J. Mason and M. Tabak, Phys. Rev. Lett. **80**, 524 (1998).
- ⁴⁸B. I. Cho, J. Osterholz, A. C. Bernstein, G. M. Dyer, A. Karmakar, A. Pukhov, and T. Ditmire, Phys. Rev. E **80**, 055402 (2009).